IOP PUBLISHING JOURNAL OF PHYSICS D: APPLIED PHYSICS

J. Phys. D: Appl. Phys. **43** (2010) 165501 (10pp) doi:10.1088/0022-3727/43/16/165501

Effective thermal conductivity of nanofluids: the effects of microstructure

Jing Fan and Liqiu Wang[1]

Department of Mechanical Engineering, the University of Hong Kong, Pokfulam Road, Hong Kong

E-mail: lqwang@hku.hk

Received 20 January 2010, in final form 23 February 2010
Published 8 April 2010
Online at stacks.iop.org/JPhysD/43/165501

Abstract

We examine numerically the effects of particle–fluid thermal conductivity ratio, particle volume fraction, particle size distribution and particle aggregation on macroscale thermal properties for seven kinds of two-dimensional nanofluids. The results show that the radius of gyration and the non-dimensional particle–fluid interfacial area are two important parameters in characterizing the geometrical structure of nanoparticles. A non-uniform particle size is found to be unfavourable for the conductivity enhancement, while particle-aggregation benefits the enhancement especially when the radius of gyration of aggregates is large. Without considering the interfacial thermal resistance, a larger non-dimensional particle–fluid interfacial area between the base fluid and the nanoparticles is also desirable for enhancing thermal conductivity. The nanofluids with nanoparticles of connected cross-shape show a much higher (lower) effective thermal conductivity when the particle–fluid conductivity ratio is larger (smaller) than 1.

(Some figures in this article are in colour only in the electronic version)

1. Introduction

Choi coined the term 'nanofluids' for fluids with nanoparticles, nanotubes or nanofibres suspended in them [1]. Recent experiments have shown their promising thermal properties such as two-fold increases in thermal conductivity [2], three-fold increases in critical heat flux (CHF) in boiling heat transfer [2–4] and substantial increases in convective heat transfer coefficient [5, 6]. However, there is still a lack of agreement between experimental results in the literature with respect to the effects of the particle size [7–11], volume fraction [7, 10–15] and temperature [7, 11, 14–16] on the thermal conductivity enhancement of nanofluids. This has attracted research on the mechanism responsible for the reported conductivity enhancement. Suggested reasons include Brownian motion of the nanoparticles [17–20], liquid-layering at the particle–liquid interface [21, 22], nanoparticle aggregation [23–26] and the nature of heat transfer at the microscale [27, 28]. At the same time, some findings tend to disqualify all these mechanisms [26, 27, 29, 30]. Therefore, our understanding on the heat conduction in nanofluids is inadequate.

The fact that the enhancement in thermal properties comes from the presence of nanoparticles has directed research efforts nearly exclusively towards thermal transport at the microscale. However, thermal conductivity is a macroscale phenomenological characterization of heat conduction and its measurements are performed at the macroscale rather than microscale. Therefore, interest should focus not only on what happens at the microscale but also on how the presence of nanoparticles affects the heat transport at the macroscale.

In an attempt to determine how the presence of nanoparticles affects the heat conduction at the macroscale and isolate the mechanisms responsible for the reported significant enhancement of thermal conductivity, a macroscale heat-conduction model in nanofluids has recently been developed by scaling up the microscale model for heat transfer in the nanoparticles and in the base fluids [15, 31]. The approach for scaling up is the volume averaging [32–34] with the help of multiscale theorems [34]. The result shows a dual-phase-lagging heat conduction in nanofluids at the macroscale [15, 31, 35, 36]. The governing equations regarding the effect of the microscale physics on macroscale thermal properties of nanofluids have also been developed [31].

This work focuses on how the nanofluid microstructure affects its effective thermal conductivity (ETC) by numerically solving the model in [31] for seven kinds of two-dimensional nanofluids. The considered microscale parameters include

[1] Author to whom any correspondence should be addressed.

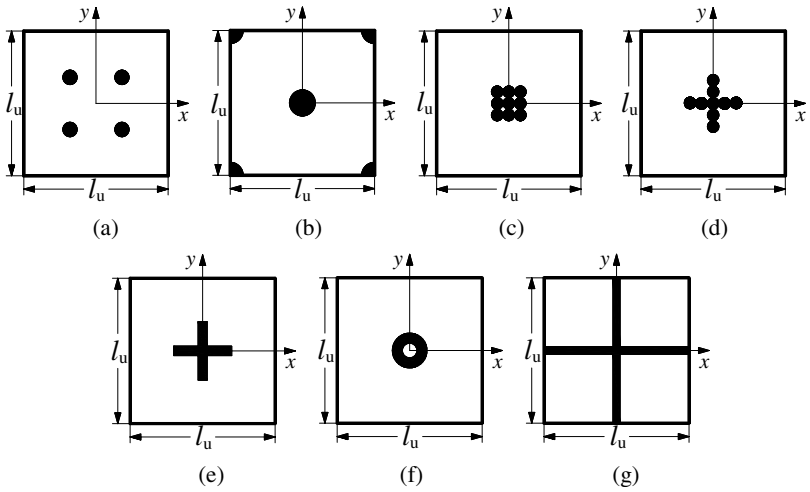

Figure 1. Unit cells for nanofluids containing in-line arrays of circular cylinders (*a*), staggered arrays of circular cylinders (*b*), in-line arrays of circular particle aggregates (*c*), (*d*), cross cylinders (*e*), hollow cylinders (*f*) and cross-particle networks (*g*).

particle–fluid thermal conductivity ratio, particle volume fraction, particle size distribution, separation distance between particles and particle-aggregation morphology. As the first attempt of such a simulation, the effect of interfacial thermal resistance and dynamic processes on particle–fluid and particle–particle interfaces is not considered. The aggregates considered in this work are limited to those that are still well dispersed in the base fluid without settling out of the fluid. Our work also centres on the microstructural effects on ETC without attempting to address or model how aggregates are formed. We limit the present simulation to the two-dimensional case with an attempt to extend it to the three-dimensional case in the future.

2. Governing equations and numerical algorithm

In this work, we use symmetric unit cells illustrated in figures 1(*a*)–(*g*) to represent nanofluids that contain in-line arrays of circular cylinders (*a*), staggered arrays of circular cylinders (*b*), circular cylinder aggregates (*c*), (*d*), cross cylinders (*e*), hollow cylinders (*f*) and cross-particle networks (*g*), respectively.

In the macroscale heat-conduction model in nanofluids [15, 31], there are five transport coefficients that represent the effects of microscale physics on macroscale heat conduction: K_{ff}, $\boldsymbol{K}_{\mathrm{fp}}$, $\boldsymbol{K}_{\mathrm{pf}}$, $\boldsymbol{K}_{\mathrm{pp}}$ and ha_{v}. For an isotropic system with constant physical properties of the two phases they reduce to scalars and are given by [15, 31, 37]

$$k_{\mathrm{ff}} = (1-\varphi)k_{\mathrm{f}} + \int_{A_{\mathrm{fp}}} \boldsymbol{n}_{\mathrm{fp}} k_{\mathrm{f}} b_{\mathrm{I}} \,\mathrm{d}A, \tag{1}$$

$$k_{\mathrm{fp}} = k_{\mathrm{pf}} = -\int_{A_{\mathrm{fp}}} \boldsymbol{n}_{\mathrm{fp}} k_{\mathrm{p}} b_{\mathrm{I}} \,\mathrm{d}A, \tag{2}$$

$$k_{\mathrm{pp}} = \varphi k_{\mathrm{p}} + \frac{k_{\mathrm{p}}}{k_{\mathrm{f}}} \int_{A_{\mathrm{fp}}} \boldsymbol{n}_{\mathrm{fp}} k_{\mathrm{p}} b_{\mathrm{I}} \,\mathrm{d}A, \tag{3}$$

$$ha_{\mathrm{v}} = \frac{\varphi}{\int_{V_{\mathrm{p}}} S \,\mathrm{d}V}. \tag{4}$$

Here k_{f} and k_{p} are the thermal conductivities of the base fluid and the particle, respectively. $\boldsymbol{n}_{\mathrm{fp}}$ is the outwardly directed unit normal vector pointing from the base fluid to the particle. φ is the particle volume fraction. A_{fp} and V_{P} are the surface area of the particle–fluid interface and the particle volume inside the unit cell. ha_{v} is the volumetric particle–fluid interfacial heat transfer coefficient, with a_{v} being the interfacial area per unit volume [31, 37]. b_{I} and S are the two closure variables that link microscale and macroscale [31, 37]. For a symmetric unit cell b_{I} and S are the solutions of the following two problems [31, 37]:

Problem I

$$\nabla \cdot (k \nabla b_{\mathrm{I}}) = -\nabla \cdot (\phi_{\mathrm{f}} k), \tag{5a}$$

$$b_{\mathrm{I}}(x + l_{\mathrm{u}}) = b_{\mathrm{I}}(x), \qquad b_{\mathrm{I}}(y + l_{\mathrm{u}}) = b_{\mathrm{I}}(y), \tag{5b}$$

$$\int_{V_{\mathrm{f}}} b_{\mathrm{I}} \,\mathrm{d}V = 0, \qquad \int_{V_{\mathrm{p}}} b_{\mathrm{I}} \,\mathrm{d}V = 0. \tag{5c}$$

Problem II

$$\nabla \cdot (k \nabla S) = -\left(\frac{\phi_{\mathrm{p}}}{\varphi} - \frac{\phi_{\mathrm{f}}}{1-\varphi}\right), \tag{6a}$$

$$S(x + l_{\mathrm{u}}) = S(x), \qquad S(y + l_{\mathrm{u}}) = S(y), \tag{6b}$$

$$\int_{V_{\mathrm{f}}} S \,\mathrm{d}V = 0, \qquad ha_{\mathrm{v}} \int_{V_{\mathrm{p}}} S \,\mathrm{d}V = \varphi. \tag{6c}$$

Here V_{f} stands for the fluid volume inside the unit cell; l_{u} represents unit-cell's dimensions in both the x- and y-directions (figure 1). ϕ_{f}, ϕ_{p} and k are defined by

$$\phi_{\mathrm{f}} = \begin{cases} 1, & \text{in } V_{\mathrm{f}}, \\ 0, & \text{in } V_{\mathrm{p}}, \end{cases} \qquad \phi_{\mathrm{p}} = \begin{cases} 0, & \text{in } V_{\mathrm{f}}, \\ 1, & \text{in } V_{\mathrm{p}}, \end{cases} \tag{7}$$

$$k = \begin{cases} k_{\mathrm{f}}, & \text{in } V_{\mathrm{f}}, \\ k_{\mathrm{p}}, & \text{in } V_{\mathrm{p}}. \end{cases} \tag{8}$$

The thermal conductivity of the two phases and the microstructure will affect the five macroscopic transport

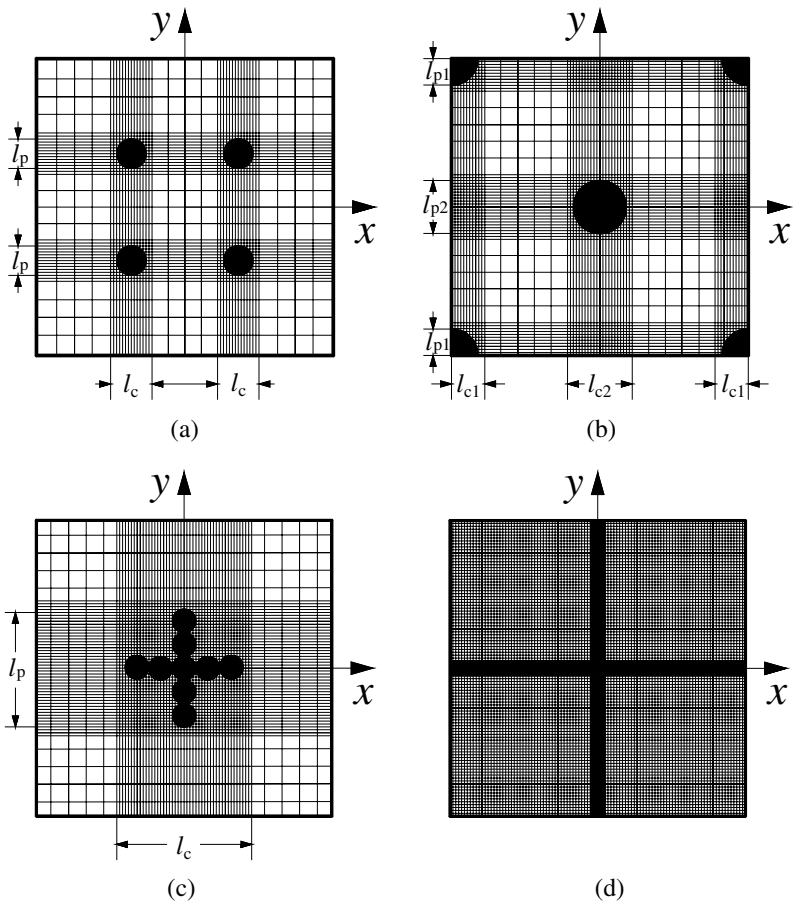

Figure 2. Grid arrangements.

coefficients—k_{ff}, k_{fp}, k_{pf}, k_{pp} and ha_v—via varying b_I and S. Furthermore, the nanofluid ETC k_e is [15, 31]

$$k_e = k_{ff} + k_{pp} + 2k_{fp}. \tag{9}$$

For unit cells that are symmetric with respect to both x and y, we have [37]

$$b_I(x, y) = b_I(x, -y), \qquad b_I(x, y) = -b_I(-x, y), \tag{10a}$$

$$S(x, y) = S(x, -y), \qquad S(x, y) = S(-x, y). \tag{10b}$$

By imposing the periodic boundary conditions (equations (5*b*) and (6*b*)), we can readily show that

$$b_I\left(-\frac{l_u}{2}, y\right) = 0, \qquad b_I\left(\frac{l_u}{2}, y\right) = 0, \tag{11a}$$

$$\frac{\partial b_I}{\partial y}\left(x, -\frac{l_u}{2}\right) = 0, \qquad \frac{\partial b_I}{\partial y}\left(x, \frac{l_u}{2}\right) = 0, \tag{11b}$$

$$\frac{\partial S}{\partial y}\left(-\frac{l_u}{2}, y\right) = 0, \qquad \frac{\partial S}{\partial y}\left(\frac{l_u}{2}, y\right) = 0, \tag{11c}$$

$$\frac{\partial S}{\partial y}\left(x, -\frac{l_u}{2}\right) = 0, \qquad \frac{\partial S}{\partial y}\left(x, \frac{l_u}{2}\right) = 0. \tag{11d}$$

Since the solutions of problems I and II are unique, we can replace the boundary conditions (5*b*) and (6*b*) by equations (11*a*)–(11*d*) without changing their final solutions.

Problems I and II with boundary conditions (11*a*)–(11*d*) are solved numerically. The numerical scheme is based on the finite volume method which is an adaptation of that in [38, 39]. The main features of this method include a central difference scheme for the diffusion terms and an equation-solving scheme consisting of an alternating-direction line-by-line iterative procedure (ADI) with the block-correction technique.

The computational grid covers the whole unit cell with a densely distributed grid in the particle region. Figures 2(*a*)–(*c*) illustrate such grids by taking the unit cells in figures 1(*a*), (*b*) and (*d*) as examples. The region width with a densely distributed grid ($l_c/l_{c1}/l_{c2}$) is about 1.5 times the dimension of particle or particle aggregate ($l_p/l_{p1}/l_{p2}$). In both regions with the densely distributed and loosely distributed grids, respectively, the grid size is uniform with the same mesh size in the x- and y-directions. We check the variation of computational results by reducing the grid size in each region into a half until the variation is less than 1% so that the results are considered to be grid-size independent. The grid numbers that yield the grid-size-independent solution are listed in tables 1 and 2. The solution is assumed to be convergent in a numerical sense if the maximum relative error in each of the computed variables over the whole grids is less than 10^{-8} between successive iterations.

The initial calculation for the unit cell containing a circular particle (figure 3) and with $\varphi = 0.2$ is performed to verify the

Table 1. Grid number used in the densely distributed grid region (N_s) and loosely distributed grid region (N_l) for problem I.

	Grid Unit cell Number (N_s : N_l)				
k_p/k_f	Figures 1(*a*) and(*b*)	Figures 1(*c*) and (*d*)	Figure 1(*e*)	Figure 1(*f*)	Figure 1(*g*)[a]
0.01, 0.02	1600/200	1600/200	1600/200	1600/200	1600/0
0.04, 0.1	800/100	800/100	800/100	800/100	1600/0
0.2–2	800/100	800/100	800/100	800/100	800/0
4,10	1600/200	1600/200	1600/200	800/100	1600/0
20,40	1600/200	3200/400	3200/400	1600/200	3200/0

[a] Densely distributed grid is used over the whole unit cell for nanofluids containing cross-particle networks as shown in figure 2(*d*).

Table 2. Grid number used in the densely distributed grid region (N_s) and loosely distributed grid region (N_l) for problem II.

	Grid Unit cell Number (N_s : N_l)				
k_p/k_f	Figure 1(*c*)	Figure 1(*d*)	Figure 1(*e*)	Figure 1(*f*)	Figure 1(*g*)[a]
0.01, 0.02	800/100	400/50	800/100	400/50	800/0
0.04–0.4	800/100	400/50	400/50	400/50	400/0
1–10	400/50	400/50	400/50	400/50	400/0
20, 40	400/50	400/50	200/26	200/26	400/0

[a] Densely distributed grid is used over the whole unit cell for nanofluids containing cross-particle networks as shown in figure 2(*d*).

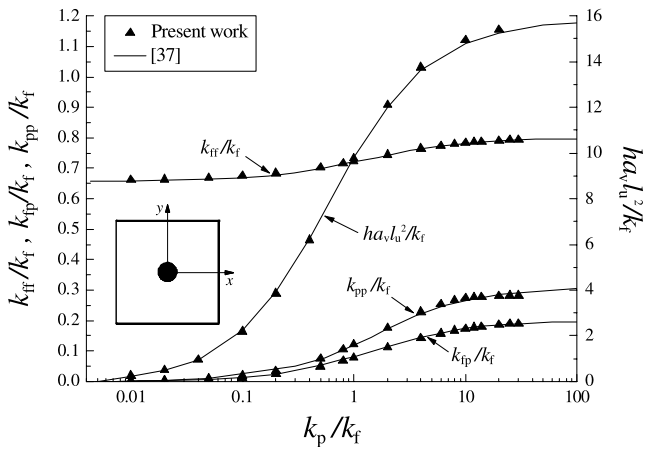

Figure 3. Comparison of macroscale effective coefficients in this work with those in [37] for the case of in-line arrays of circular cylinders at $\varphi = 0.2$.

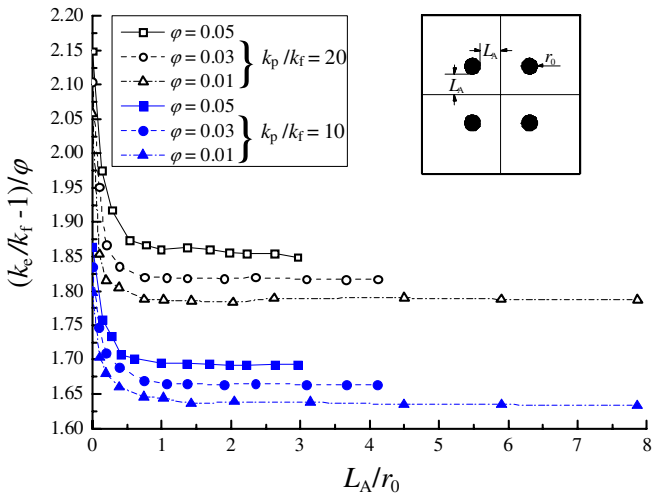

Figure 4. Non-dimensional thermal conductivity $(k_e/k_f - 1)/\varphi$ as a function of the relative distance L_A/r_0, particle volume fraction φ and thermal conductivity ratio k_p/k_f.

code and the accuracy. The variations of k_{ff}/k_f, k_{fp}/k_f, k_{pp}/k_f and $ha_v l_u^2/k_f$ with k_p/k_f are shown and compared with those in [37] in figure 3, showing an excellent agreement between our results and those in [37].

3. Results and discussion

3.1. Effect of particle aggregation

The effects of particle aggregation on ETC of nanofluids are examined by changing the relative separation distance between four circular particles defined by L_A/r_0 (figure 1(*a*)). Here r_0 and L_A are the particle radius and the distance between one particle and the centreline of unit cell, respectively (figure 4). The case of uniformly dispersed in-line arrays of circular cylinders corresponds to a maximum value of L_A/r_0 fixed by the particle volume fraction. When $L_A/r_0 = 0$, the four particles touch with each other to form an aggregate and such aggregates disperse uniformly in the base fluids. Figure 4 shows the variation of the non-dimensional thermal conductivity $(k_e/k_f - 1)/\varphi$ as a function of the relative distance L_A/r_0, particle volume fraction φ and thermal conductivity ratio k_p/k_f. The $(k_e/k_f - 1)/\varphi$ decreases sharply with increasing L_A/r_0 when the relative distance L_A/r_0 is less than 1, but is nearly independent of L_A/r_0 when L_A/r_0 is larger than 1. Therefore, the effect of particle aggregation on the ETC would become effective and observable when the distance between particles is less than the particle dimension. The $(k_e/k_f - 1)/\varphi$ also increases with an increase in either the particle volume fraction φ or the thermal conductivity ratio k_p/k_f.

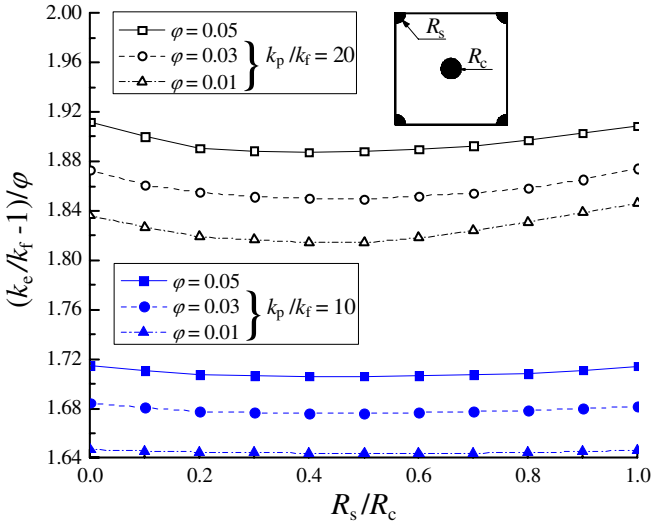

Figure 5. Non-dimensional thermal conductivity $(k_e/k_f - 1)/\varphi$ as a function of the radius ratio R_s/R_c, particle volume fraction φ and thermal conductivity ratio k_p/k_f.

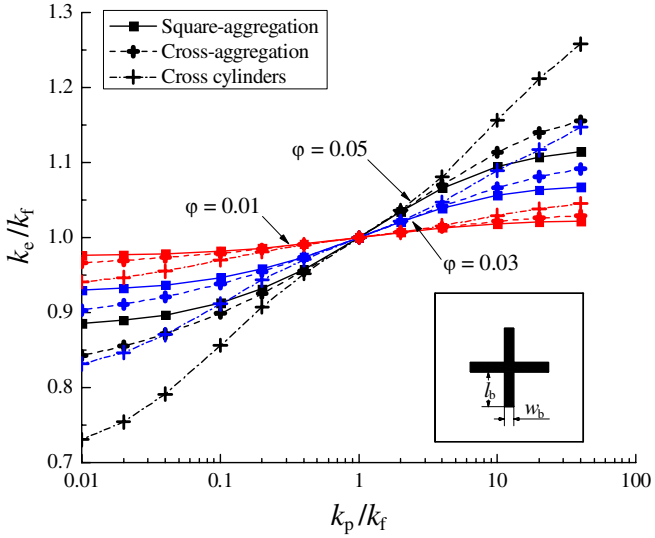

Figure 6. ETC ratio k_e/k_f as a function of particle-aggregation morphology, k_p/k_f and φ.

3.2. *Effect of particle size distribution*

To examine the effects of particle size distribution on the ETC, we vary R_s/R_c (the radius ratio of four corner particles to the centre particle in figure 1(*b*)) from 0 to 1. When $R_s/R_c = 0$, nanofluids consist of in-line arrays of uniform-sized circular cylinders. When $R_s/R_c = 1$, nanofluids contain staggered arrays of uniform-sized circular cylinders. Figure 5 typifies the variation of non-dimensional thermal conductivity $(k_e/k_f - 1)/\varphi$ with R_s/R_c, showing that a variation of R_s/R_c from either 0 or 1 decreases $(k_e/k_f - 1)/\varphi$. Therefore, the uniformly distributed particle size is preferable for achieving a higher non-dimensional thermal conductivity. Compared with the effect of the particle aggregation shown in figure 4, however, the effect of particle size distribution is very weak (figure 5).

3.3. *Effect of particle-aggregation morphology*

Figure 6 shows the ETC ratio k_e/k_f for the three different particle-aggregation morphologies (square-aggregation in figure 1(*c*), cross-aggregation in 1(*d*) and cross particle in 1(*e*), respectively). Both figures 1(*c*) and (*d*) represent aggregates of nine equal-sized circular particles. For the fixed particle volume fraction, therefore, the non-dimensional particle–fluid interfacial area in the unit cell (defined in table 3; all lengths being normalized by the unit cell's dimension l_u) is the same for both cases (our previous study has shown a significant dependence of k_e/k_f on this non-dimensional interfacial area [40]). Due to the different aggregation morphology, however, the radius of gyration R_g defined by the root mean square distance of the aggregate's parts from its centre [41] is larger for the aggregate in figure 1(*d*). For the same non-dimensional particle–fluid interfacial area as that for the square-aggregation in figure 1(*c*) and the cross-aggregation in 1(*d*), we specify the dimensions of the cross particle in figure 1(*e*) by

$$\frac{w_b}{l_u} = \frac{3\sqrt{\pi\varphi} - \sqrt{9\pi\varphi - 4\varphi}}{2}, \tag{12}$$

$$\frac{l_b}{l_u} = \frac{\varphi - (w_b/l_u)^2}{4\,(w_b/l_u)}. \tag{13}$$

Here w_b and l_b are the width and length of the cross particle branch shown in figure 6, respectively. Obviously, the branch width w_b is smaller than the diameter of the circular particle in the aggregates in figures 1(*c*) and (*d*) so that the radius of gyration in figure 1(*e*) is larger than that in either figures 1(*c*) or (*d*).

The value of k_e/k_f is nearly independent of particle-aggregation morphology around $k_p/k_f = 1$ (figure 6). When k_p/k_f is smaller than 1, k_e/k_f has the lowest value for the cross particle in figure 1(*e*) and the highest value for the square-aggregation in figure 1(*c*). When k_p/k_f is larger than 1, however, k_e/k_f has the highest value for the cross particle in figure 1(*e*) and the lowest value for the square-aggregation in figure 1(*c*). Therefore, the effect of particle-aggregation morphology varies with the particle–fluid conductivity ratio. An upgrade of the radius of gyration from figures 1(*c*) to 1(*e*) by changing the particle-aggregation morphology will decrease k_e/k_f when $k_p/k_f \leqslant 1$ but increase k_e/k_f when $k_p/k_f \geqslant 1$. Furthermore, the sensitivity of k_e/k_f to the particle-aggregation morphology becomes stronger as the particle volume fraction φ increases (figure 6).

The ETC ratio k_e/k_f increases with increasing particle–fluid conductivity ratio k_p/k_f. The dependence of k_e/k_f on k_p/k_f becomes stronger with an increase in the particle volume fraction φ. The sensitivity of k_e/k_f to k_p/k_f becomes stronger from the square-aggregation in figure 1(*c*) to the cross-aggregation in 1(*d*) and the cross particle in 1(*e*). For both the square-aggregation in figure 1(*c*) and the cross-aggregation in 1(*d*), k_e/k_f tends towards a lower limit for very small k_p/k_f and a higher limit for very large k_p/k_f (figure 6). Both the lower and the higher limits depend on the particle volume fraction and the aggregation morphology.

Table 3. Non-dimensional particle–fluid interfacial areas in the unit cell for nanofluids in figures 1(*c*)–(*f*).

Particles/aggregates	Non-dimensional particle–fluid interfacial area in unit cell
Figure 1(*c*)	$9 \cdot 2\pi(r/l_u) = 6\sqrt{\pi\varphi}$; r is the radius of the small circular particles, particle volume fraction $\varphi = 9 \cdot \pi\,(r/l_u)^2$.
Figure 1(*d*)	$9 \cdot 2\pi\,(r/l_u) = 6\sqrt{\pi\varphi}$; r is the radius of the small circular particles, particle volume fraction $\varphi = 9 \cdot \pi\,(r/l_u)^2$.
Figure 1(*e*)	$4 \cdot ((2l_b + w_b)/l_u) = 2 \cdot ((\varphi + (w_b/l_u)^2)/(w_b/l_u))$; particle volume fraction $\varphi = 2 \cdot (w_b/l_u) \cdot (2l_b + w_b)/l_u - (w_b/l_u)^2$.
Figure 1(*f*)	$2\pi\,((R_0/l_u) + (R_0 - w_h)/l_u) = 2\sqrt{(2(R_0/w_h) - 1) \cdot \pi\varphi}$; particle volume fraction $\varphi = \pi\,(R_0/l_u)^2 - \pi((R_0 - w_h)/l_u)^2$.

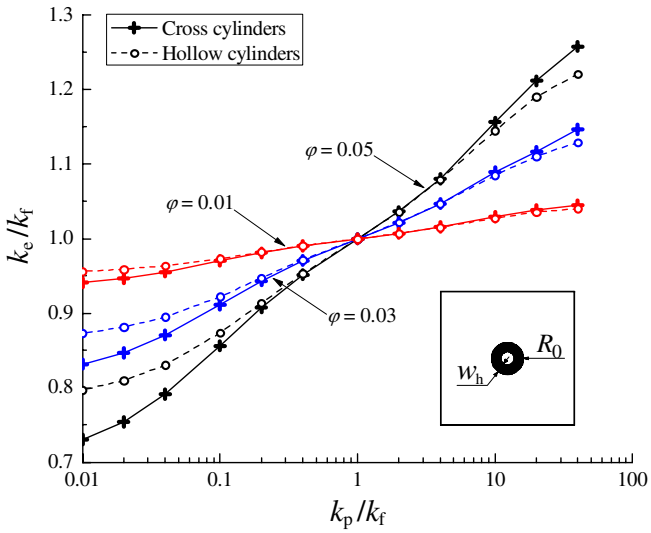

Figure 7. ETC k_e/k_f as a function of k_p/k_f and φ for two particles with the same radius of gyration but different non-dimensional particle–fluid interfacial area.

3.4. Effect of non-dimensional particle–fluid interfacial area

For the effect of non-dimensional particle–fluid interfacial area (table 3) on the nanofluid ETC, we compare the ETC ratio k_e/k_f for nanofluids in figures 1(*e*) and (*f*) in figure 7. In our simulation, we keep the same particle volume fraction φ and radius of gyration for both types of nanofluids by determining the dimensions of hollow particle in figure 1(*f*) by

$$\pi\left(\frac{R_0}{l_u}\right)^2 - \pi\left(\frac{R_0 - w_h}{l_u}\right)^2 = \varphi, \tag{14}$$

$$\frac{\left(2\frac{l_b}{l_u} + \frac{w_b}{l_u}\right)^3 \frac{w_b}{l_u} + \left(2\frac{l_b}{l_u} + \frac{w_b}{l_u}\right)\left(\frac{w_b}{l_u}\right)^3 - \left(\frac{w_b}{l_u}\right)^4}{6\varphi} = \frac{\left(\frac{R_0}{l_u}\right)^2 + \left(\frac{R_0}{l_u} - \frac{w_h}{l_u}\right)^2}{2}. \tag{15}$$

Here R_0 and w_h are the outside radius and the wall-thickness of the hollow particle, respectively (figure 7). The non-dimensional particle–fluid interfacial area of the cross particle is about 9% larger than that of the hollow particle. For the cross particle in figure 1(*e*), the ETC ratio k_e/k_f is lower when k_p/k_f is smaller than 1 and higher when k_p/k_f is larger than 1. Therefore, the effect of non-dimensional particle-fluid interfacial area varies with the particle–fluid conductivity ratio. A downgrade of the non-dimensional interfacial area from figures 1(*e*) to 1(*f*) will increase k_e/k_f when $k_p/k_f \leqslant 1$ but decrease k_e/k_f when $k_p/k_f \geqslant 1$. The sensitivity of k_e/k_f to the non-dimensional interfacial area becomes stronger as the particle volume fraction φ increases (figure 7). Also, k_e/k_f increases as k_p/k_f increases and its k_p/k_f-dependence is stronger for the nanofluids with cross particles in figure 1(*e*) (figure 7).

Here the non-dimensional particle–fluid interfacial area differs from the particle surface-to-volume ratio. For a fixed value of the particle volume fraction, the former depends on the particle shape so that we can use it to characterize the effect of particle shape. The latter is useful for characterizing the effect of particle size. The particle size could affect the ETC of nanofluids through various means such as the particle Brownian motion [17], the particle thermal conductivity [9], the interfacial thermal resistance [9] and even the particle aggregating process and the geometrical structure of the aggregates [24]. The readers are referred to [24] for a good review and discussion of the role of particle size in varying nanofluid thermal conductivity.

3.5. Parameters for characterizing effects of particles' geometrical structures

To address whether we can characterize the effects of particles' geometrical structures by using their radius of gyration and non-dimensional particle–fluid interfacial area in the unit cell, we examine the four macroscale thermal coefficients and the ETC ratio in figure 8 for nanofluids containing the cross and hollow particles, respectively (figures 1(*e*) and (*f*)), at $\varphi = 0.05$. For the same radius of gyration and non-dimensional interfacial area for both cases, we fix the dimensions of cross and hollow particles by equations (13)–(16):

$$4 \cdot \frac{2l_b + w_b}{l_u} = 2\pi\left(\frac{R_0}{l_u} + \frac{R_0 - w_h}{l_u}\right). \tag{16}$$

Figure 8 clearly shows that the four macroscale thermal coefficients and the ETC ratio are almost the same for two particles. Therefore, the radius of gyration and non-dimensional interfacial area are two very important parameters to characterize the effects of particles' geometrical structures.

It is interesting to note that well-controlled linear aggregates can be generated along the direction of heat flux in Fe_3O_4 based nanofluids under an applied external magnetic field [24]. The experimental data regarding the effect of the aspect ratio of such linear aggregates are also available

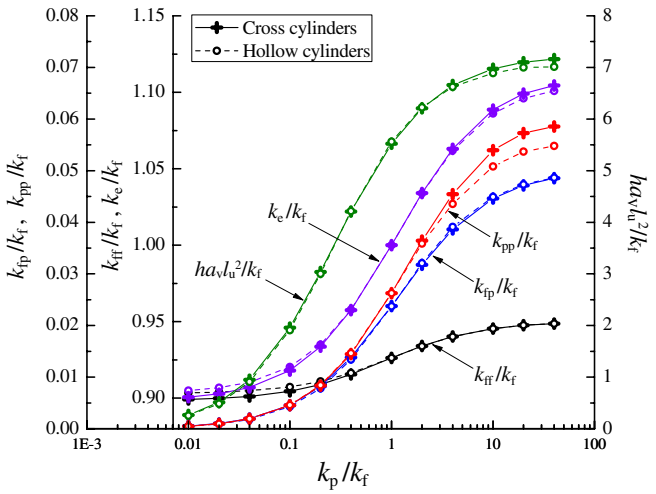

Figure 8. Macroscale thermal coefficients for the two particles with the same non-dimensional particle–fluid interfacial area, radius of gyration and volume fraction ($\varphi = 0.05$).

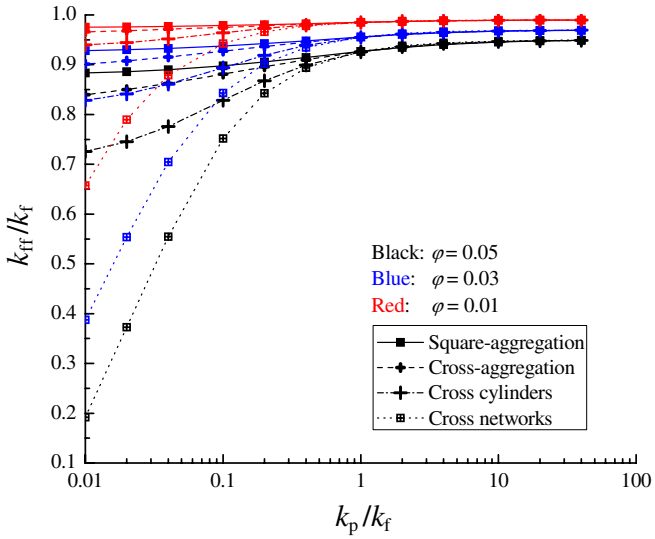

Figure 9. Non-dimensional thermal coefficient k_{ff}/k_f as a function of particle-aggregation morphology, k_p/k_f and φ.

in [24]. Note that the nanofluids with such linear aggregates are anisotropic with a direction-dependent ETC. It would be very interesting to perform a numerical simulation for such anisotropic nanofluids with asymmetric unit cells and make a comparison with the available experimental data in [24] in the future. In that case, problems I and II are different from the ones used in this work [31, 37].

3.6. Four macroscale thermal coefficients and the case of infinite radius of gyration

Note that particles with a large radius of gyration are beneficial for the enhancement of the ETC when the particles have a higher thermal conductivity than the base fluids (figure 6). To confirm this further, we compute the four macroscale thermal coefficients and the ETC ratio for nanofluids consisting of the cross-particle network shown in figure 1(g) which has an infinite radius of gyration and compare the results with those for square-aggregation in figure 1(c), cross-aggregation in figure 1(d) and cross particle in figure 1(e).

Figure 9 shows the variation of the non-dimensional thermal coefficient k_{ff}/k_f as a function of the particle-aggregation morphology, thermal conductivity ratio k_p/k_f and particle volume fraction φ. The coefficient k_{ff}/k_f is nearly independent of the particle-aggregation morphology when k_p/k_f is larger than 1, but experiences a significant decrease when $k_p/k_f \leqslant 1$ in response to the change in particle-aggregation morphology from the square-aggregation in figure 1(c) to the cross-aggregation in 1(d), the cross particle in 1(e) and the cross-particle network in figure 1(g). Its sensitivity to the particle-aggregation morphology becomes stronger as the particle volume fraction φ increases. As k_p/k_f increases towards infinity, the coefficient k_{ff}/k_f increases and tends to a limit value of $(1 - \varphi)$. Also, the k_p/k_f-sensitivity becomes stronger as particle-aggregation morphology shifts from the square-aggregation in figure 1(c) and the cross-aggregation in figure 1(d) to the cross particle in figure 1(e) and the cross-particle network in figure 1(g) (figure 9). As the particle volume fraction φ increases, however, the coefficient k_{ff}/k_f decreases considerably.

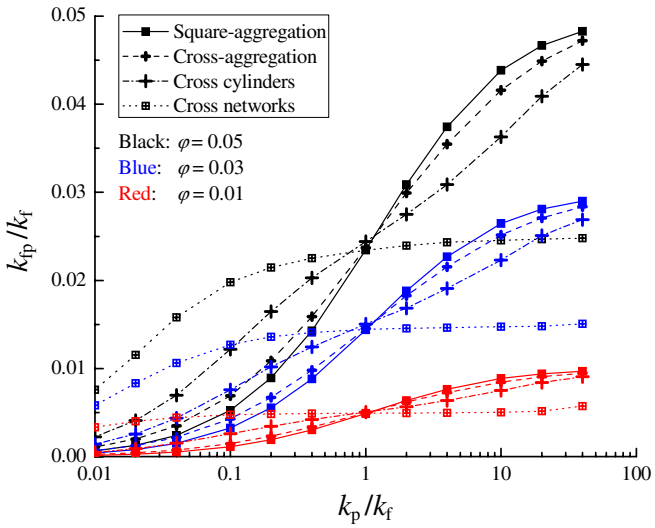

Figure 10. Non-dimensional thermal coefficient k_{fp}/k_f as a function of particle-aggregation morphology, k_p/k_f and φ.

Figure 10 illustrates the variation of the non-dimensional coefficient k_{fp}/k_f with the particle-aggregation morphology, the thermal conductivity ratio k_p/k_f and the particle volume fraction φ. Similarly, the k_{fp}/k_f for the cross-particle network differs considerably from those for the square-aggregation in figure 1(c) and the cross-aggregation in figure 1(d) and the k_{fp}/k_f for the cross particle in figure 1(e) falls in between. The k_{fp}/k_f for the cross-particle network is much higher than the others when k_p/k_f is smaller than 1 and much lower when k_p/k_f is larger than 1. The sensitivity to the particle-aggregation morphology becomes stronger as the particle volume fraction φ increases. Also, the coefficient k_{fp}/k_f increases as k_p/k_f increases. For both the square-aggregation in figure 1(c) and the cross-aggregation in figure 1(d), the k_{fp}/k_f tends towards 0 as k_p/k_f decreases to 0 and towards a limit value of φ as

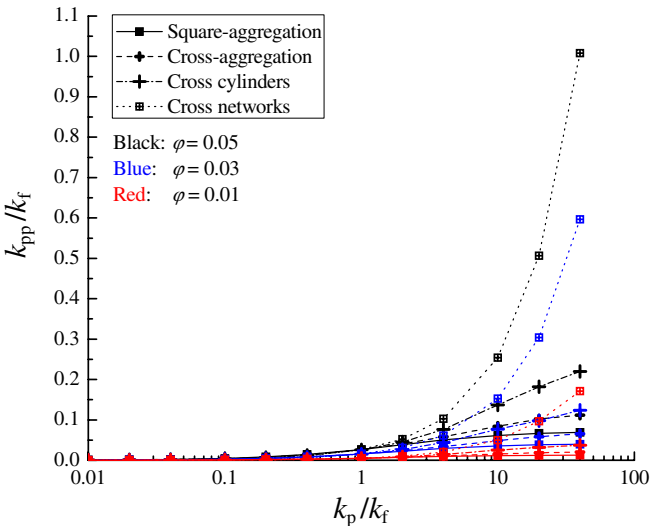

Figure 11. Non-dimensional thermal coefficient k_{pp}/k_f as a function of particle-aggregation morphology, k_p/k_f and φ.

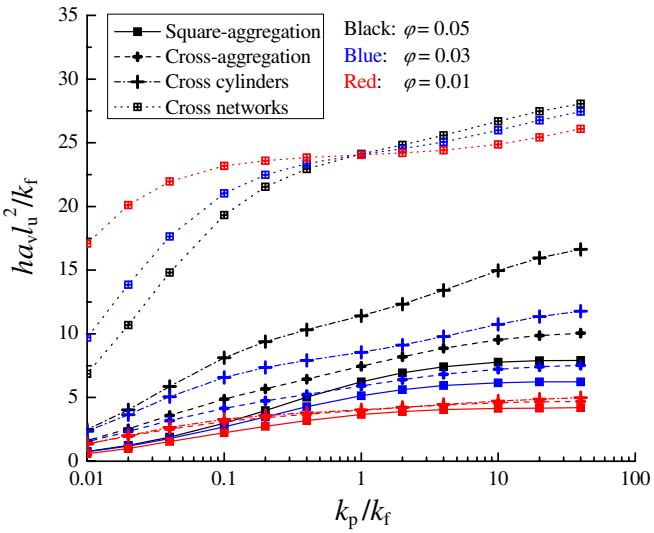

Figure 12. Non-dimensional heat transfer coefficient $ha_v l_u^2/k_f$ as a function of particle-aggregation morphology, k_p/k_f and φ.

k_p/k_f increases to infinity. The variation of k_{fp}/k_f with k_p/k_f becomes more significant as φ increases. Moreover, as the particle volume fraction φ increases, the coefficient k_{fp}/k_f increases significantly.

The variation of k_{pp}/k_f with the microstructure is shown in figure 11. It is nearly independent of the particle-aggregation morphology when k_p/k_f is less than 1 and increases significantly when k_p/k_f is larger than 1 in response to the change in particle-aggregation morphology from the square-aggregation in figure 1(*c*) and the cross-aggregation in figure 1(*d*) to the cross particle in figure 1(*e*) and the cross-particle network in figure 1(*g*) (figure 11). Its sensitivity to the particle-aggregation morphology becomes stronger as the particle volume fraction φ increases. As k_p/k_f increases from 0 to infinity and for the square-aggregation in figure 1(*c*) and the cross-aggregation in figure 1(*d*), the coefficient k_{pp}/k_f increases from 0 to a limit value that depends on the aggregation morphology and the particle volume fraction. For the cross-particle network in figure 1(*g*), however, k_{pp}/k_f tends to increase sharply with k_p/k_f when k_p/k_f is larger than 1 although k_{pp}/k_f increases with increasing k_p/k_f and has a lower limit of 0. The change in k_{pp}/k_f with k_p/k_f becomes more significant as φ increases. As the particle volume fraction φ increases, the coefficient k_{pp}/k_f also increases significantly.

Figure 12 shows the variation of the non-dimensional heat transfer coefficient $ha_v l_u^2/k_f$. It increases significantly as the particle-aggregation morphology changes from the square-aggregation in figure 1(*c*) to the cross-aggregation in figure 1(*d*), the cross particle in figure 1(*e*) and the cross-particle network in figure 1(*g*) (figure 12). The coefficient $ha_v l_u^2/k_f$ for the cross network in figure 1(*g*) is much higher than the others (figure 12). Also, the $ha_v l_u^2/k_f$ increases as k_p/k_f increases, with the sensitivity becoming stronger as the particle-aggregation morphology changes from the square-aggregation in figure 1(*c*) and the cross-aggregation in figure 1(*d*) to the cross particle in figure 1(*e*) and the cross-particle network in figure 1(*g*). An upgrade of the particle volume fraction φ yields a significant increase in $ha_v l_u^2/k_f$

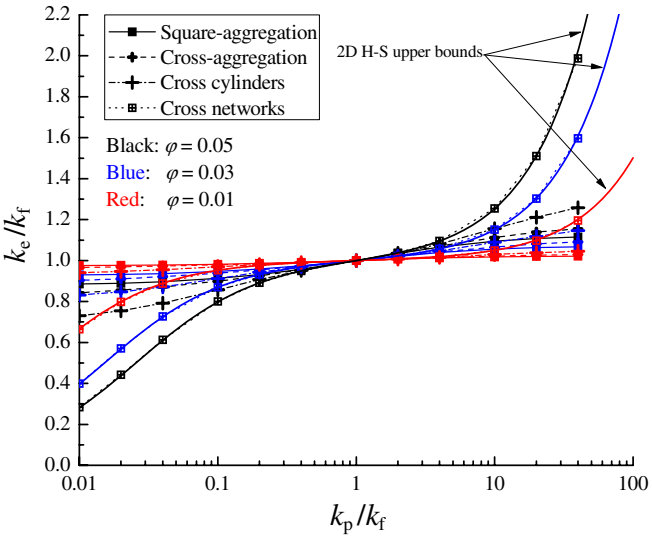

Figure 13. ETC k_e/k_f as a function of particle-aggregation morphology, k_p/k_f and φ.

for the first three types of nanofluids. However, $ha_v l_u^2/k_f$ for the cross-particle network in figure 1(*g*) shows a different behaviour and it increases with φ when k_p/k_f is larger than 1 and decreases with φ when k_p/k_f is less than 1.

Finally, in figure 13, the ETC of the cross-particle network suspensions is compared with those of the other three suspensions and the two-dimensional Hashin–Shtrikman (H–S) bounds (for macroscopically homogeneous and isotropic systems, [42])

$$k_e/k_f = k_p/k_f \left[1 - \frac{2(1-\varphi)(k_p/k_f - 1)}{2k_p/k_f - \varphi(k_p/k_f - 1)}\right]. \quad (17)$$

The H–S bound, given by equation (17), is the most restrictive upper bound when k_p/k_f is larger than 1 and the most restrictive lower bound when k_p/k_f is less than 1.

The ETC for the nanofluids with the connected cross-particle network in figure 1(*g*) is much higher than the other

three types of nanofluids when k_p/k_f is larger than 1 and much lower when k_p/k_f is less than 1. Their conductivity can practically reach the 2D H–S bound (figure 13). Therefore, future efforts should focus on the synthesis of nanofluids containing particles/aggregates with large radius of gyration and large non-dimensional interfacial area to maximize the effect of added particles on the conductivity enhancement.

4. Concluding remarks

The macroscopic heat-conduction behaviour and the thermal conductivity of nanofluids are determined by the molecular and microscale physics in them, including material properties of nanoparticles and base fluids, nanoparticles' geometrical structures and their distribution in the base fluids and interfacial properties and dynamic processes on particle–fluid interfaces. This work examines numerically how microscale physics affects the ETC for nanofluids containing two-dimensional circular, cross and hollow particles, circular particle aggregates and connected cross-particle networks, without considering interfacial thermal resistance and dynamic processes on particle–fluid interfaces and particle–particle contacting surface.

The simulation results on nanofluids containing in-line arrays of circular cylinders show that particle aggregation affects the ETC only when the distance between particles is less than the particle dimension.

Uniformly sized particles are desirable for the conductivity enhancement. Although particle aggregation probably leads to non-uniform suspended aggregate sizes in practice and thus yields a negative effect on the conductivity enhancement, the positive effect of particle aggregation is much stronger than its negative effect.

The non-dimensional particle–fluid interfacial area and the particles' radius of gyration are two very important parameters to characterize the effect of particles' geometrical structures on thermal conductivity of nanofluids. The particle aggregation with a larger radius of gyration and large non-dimensional interfacial area is more beneficial to the conductivity enhancement. The ETC for nanofluids with connected cross-particle network can practically reach the two-dimensional H–S upper bound (when $k_p/k_f > 1$) and lower bound (when $k_p/k_f < 1$).

Acknowledgment

The financial support from the Research Grants Council of Hong Kong (GRF718009) is gratefully acknowledged.

References

[1] Choi S U S 1995 Enhancing thermal conductivity of fluids with nanoparticles *Developments and Applications of Non-Newtonian Flows* ed D A Singer and H P Wang (New York: ASME) vol FED 231 pp 99–105

[2] Peterson G P and Li C H 2006 Heat and mass transfer in fluids with nanoparticle suspensions *Adv. Heat Transfer* (New York: Academic) **39** 257–376

[3] Das S K, Choi S U S, Yu W H and Pradeep T 2008 *Nanofluids: Science and Technology* (New Jersey: Wiley)

[4] Choi S U S, Zhang Z G and Keblinski P 2004 Nanofluids *Encyclopedia of Nanoscience and Nanotechnology* ed H S Nalwa (New York: American Scientific Publishers) vol 6 pp 757–73

[5] Wen D S, Ding Y L and Williams R 2005 Nanofluids turn up the heat *Chem. Eng.* **771** 32–4

[6] Tzou D Y 2008 Thermal instability of nanofluids in natural convection *Int. J. Heat Mass Transfer* **51** 2967–79

[7] Li C H and Peterson G P 2007 The effect of particle size on the effective thermal conductivity of Al_2O_3–water nanofluids *J. Appl. Phys.* **101** 044312

[8] Kim S H, Choi S R and Kim D 2007 Thermal conductivity of metal-oxide nanofluids: Particle size dependence and effect of laser irradiation *ASME J. Heat Transfer* **129** 298–307

[9] Beck M P, Yuan Y H, Warrier P and Teja A S 2009 The effect of particle size on the thermal conductivity of alumina nanofluids *J. Nanopart. Res.* **11** 1129–36

[10] Chopkar M, Sudarshan S, Das P K and Manna I 2008 Effect of particle size on thermal conductivity of nanofluids *Metall. Mater. Trans.* A **39** 1535–42

[11] Mintsa H A, Roy G, Nguyen C T and Doucet D 2009 New temperature dependent thermal conductivity data for water-based nanofluids *Int. J. Therm. Sci.* **48** 363–71

[12] Eastman J A, Choi S U S, Li S, Yu W and Thompson L J 2001 Anomalously increased effective thermal conductivities of ethylene glycol-based nanofluids containing copper nanoparticles *Appl. Phys. Lett.* **78** 718–20

[13] Choi S U S, Zhang Z G, Yu W, Lockwood F E and Grulke E A 2001 Anomalous thermal conductivity enhancement in nanotube suspensions *Appl. Phys. Lett.* **79** 2252–4

[14] Wei X H, Zhu H T, Kong T T and Wang L Q 2009 Synthesis and thermal conductivity of Cu_2O Nanofluids *Int. J. Heat Mass Transfer* **52** 4371–4

[15] Wang L Q and Wei X H 2009 Nanofluids: synthesis, heat conduction, and extension *ASME J. Heat Transfer* **131** 033102

[16] Das S K, Putra N, Thiesen P and Roetzel W 2003 Temperature dependence of thermal conductivity enhancement for nanofluids *ASME J. Heat Transfer* **125** 567–74

[17] Jang S P and Choi S U S 2004 Role of Brownian motion in the enhanced thermal conductivity of nanofluids *Appl. Phys. Lett.* **84** 4316–8

[18] Koo J and Kleinstreuer C 2004 A new thermal conductivity model for nanofluids *J. Nanopart. Res.* **6** 577–88

[19] Xu J, Yu B M, Zou M Q and Xu P 2006 A new model for heat conduction of nanofluids based on fractal distributions of nanoparticles *J. Phys. D: Appl. Phys.* **39** 4486–90

[20] Xie H, Wang J, Xi T, Liu Y and Ai F 2002 Thermal conductivity enhancement of suspensions containing nanosized alumina particles *J. Appl. Phys.* **91** 4568–72

[21] Yu W and Choi S U S 2003 The role of interfacial layers in the enhanced thermal conductivity of nanofluids: A renovated Maxwell model *J. Nanoparticle Res.* **5** 167–71

[22] Ren Y, Xie H and Cai A 2005 Effective thermal conductivity of nanofluids containing spherical nanoparticles *J. Phys. D: Appl. Phys.* **38** 3958–61

[23] Philip J, Shima P D and Raj B 2008 Evidence for enhanced thermal conduction through percolating structures in nanofluids *Nanotechnology* **19** 305706

[24] Shima P D, Philip J and Raj B 2009 Role of microconvection induced by Brownian motion of nanoparticles in the enhanced thermal conductivity of stable nanofluids *Appl. Phys. Lett.* **94** 223101

[25] Gao L, Zhou X and Ding Y 2007 Effective thermal and electrical conductivity of carbon nanotube composites *Chem. Phys. Lett.* **434** 297–300

[26] Keblinski P, Prasher R and Eapen J 2008 Thermal conductance of nanofluids: is the controversy over? *J. Nanopart. Res.* **10** 1089–97
[27] Keblinski P, Phillpot S R, Choi S U S and Eastman J A 2002 Mechanisms of heat flow in suspensions of nano-sized particles (nanofluids) *Int. J. Heat Mass Transfer* **45** 855–63
[28] Eapen J, Li J and Yip S 2007 Mechanism of thermal transport in dilute nanocolloids *Phys. Rev. Lett.* **98** 028302
[29] Xue L, Keblinski P, Phillpot S R, Choi S U S and Eastman J A 2004 Effect of liquid layering at the liquid–solid interface on thermal transport *Int. J. Heat Mass Transfer* **47** 4277–84
[30] Buongiorno J *et al* 2009 A benchmark study on the thermal conductivity of nanofluids *J. Appl. Phys.* **106** 094312
[31] Wang L Q and Quintard M 2009 Nanofluids of the future *Advances in Transport Phenomena* ed L Q Wang (New York: Springer) pp 179–243
[32] Whitaker S 1999 *The Method of Volume Averaging* (Dordrecht: Kluwer)
[33] Wang L Q 2000 Flows through porous media: a theoretical development at macroscale *Trans. Porous Media* **39** 1–24
[34] Wang L Q, Xu M T and Wei X H 2008 Multiscale theorems *Adv. Chem. Eng.* **34** 175–468
[35] Tzou D Y 1997 *Macro- to Microscale Heat Transfer: The Lagging Behavior* (Washington, DC: Taylor and Francis)
[36] Wang L Q, Zhou X S and Wei X H 2008 *Heat Conduction: Mathematical Models and Analytical Solutions* (Heidelberg: Springer)
[37] Quintard M and Whitaker S 1993 One- and two- equation models for transient diffusion processes in two-phase systems *Adv. Heat Transfer* (New York: Academic) **23** 369–471
[38] Wang L Q and Yang T L 2004 Multiplicity and stability of convection in curved ducts: review and progress *Adv. Heat Transfer* (New York: Academic) **38** 203–55
[39] Wang L Q and Cheng K C 1996 Flow transitions and combined free and forced convective heat transfer in rotating curved channels: the case of positive rotation *Phys. Fluids* **8** 1553–73
[40] Fan J and Wang L Q 2010 Microstructural effects on macroscale thermal properties in nanofluids *NANO* at press
[41] Goldstein H 1980 *Classical Mechanics* (Reading, MA: Addison-Wesley)
[42] Hashin Z and Shtrikman S 1962 A variational approach to the theory of the effective magnetic permeability of multiphase materials *J. Appl. Phys.* **33** 3125–31